Proton-Induced Secondary Particle Environment for Infrared Sensor Applications*

James C. Pickel,[1] *Fellow, IEEE,* Robert A. Reed,[2] *Member, IEEE,* Paul W. Marshall,[3] *Member, IEEE,* Tom M. Jordan,[4] *Member, IEEE,* George Gee[5], *Member, IEEE*, Bryan Fodness,[5] *Member, IEEE*, Mark McKelvey,[6] Robert E. McMurray,[6] Kim A. Ennico,[6] Roy R. Johnson[6] and Craig McCreight[6]

Abstract--**We present measurements of the proton-induced secondary particle environment in the vicinity of an infrared focal plane array. Measurements were made of the energy depositions from secondary electrons and scattered protons from the interior of a cryogenic test dewar using an infrared detector array. The results are compared to model predictions and analyzed for implications to space-based infrared sensors.**

I. INTRODUCTION

Space-based infrared detectors are required to operate in the ionizing particle environments of space. Infrared detectors are also efficient ionizing particle detectors, and the single event transients from energetic particles are captured on the integration nodes of detector array pixels and remain until the array is reset at the end of the integration time. Shielding is not an effective option due to the high energies of the particles and due to secondary particle generation when passing through shielding. The very low noise floor of a few electrons in modern infrared detector arrays implies that essentially every secondary particle that reaches the sensitive volume of the focal plane array (FPA) generates detectable charge that adds to the primary particle charge and contributes to the noise floor. Small noise charges that are near the noise floor cannot be removed by signal processing and are problematic for sensitive applications such as space-based IR astronomy.

There is experimental evidence of secondary particles interfering with IR telescopes from the on-orbit experience of the European Space Agency's Infrared Space Observatory (ISO) [1]. Measurement of transients in the ISO detectors indicated a transient rate approximately 80 % higher than could be accounted for by the primary particles. The higher than expected transient rate was attributed to secondary particles and delta electrons. In addition, the possible role of secondary particles in the performance of the Near Infrared Camera Multi-Object Spectrometer (NICMOS) camera has been studied [2].

NASA's James Webb Space Telescope (JWST) Program is investigating potential transient effects on prototype FPA hardware through modeling and testing [3]. As an auxiliary experiment during the course of proton testing of JWST prototype IR detector arrays, we measured the secondary particle environment that is generated in the vicinity of an IR detector inside a cryogenic test dewar. The secondary environment consists primarily of secondary electrons (often termed delta electrons) and scattered protons, and is generated by the test dewar material near the detector. The detector array had the substrate removed so there was no 'dead' layer to shield low range, but high linear energy transfer (LET) secondary particles. Also the detector is in a vacuum within the test dewar. These conditions allowed us to obtain energy deposition spectra for the secondary particles by measuring the charge generation within the pixels of the detector array.

James C. Pickel is with PR&T, Inc., Fallbrook, CA. (telephone: 760-451-2256, e-mail: jim@pickel.net)

Robert A. Reed is with NASA/GSFC, Greenbelt, MD.

Paul W. Marshall is a Consultant with NASA/GSFC, Greenbelt, MD.

Tom M. Jordan is with EMP Consultants.

George Gee and Bryan Fodness are with SGT, Inc.

Mark McKelvey, Robert E. McMurray, Kim A. Ennico, Roy R. Johnson and Craig McCreight are with NASA Ames Research Center.

II. Experimental Approach

Testing was performed at the University of California Davis (UCD) cyclotron using a 63 MeV proton beam. The proton beam was collimated to 1 inch diameter using an Al collimator. Collimation was verified by exposing radio-chromic film and noting the sharp edge between exposed and unexposed regions. Beam dosimetry at the facility provided flux and total fluence data. The purpose of this particular set of experiments was to evaluate the instantaneous secondary particle emission from a material sample near the detector while the proton beam was on the sample with a moderate flux comparable to the fluxes that were used in single event transient testing of detectors. An additional goal was to evaluate the latent particle emissions from decay of the activated sample after a large proton fluence. In this paper, we are reporting only on the instantaneous secondary particle results.

The particular material sample that was evaluated for these measurements was an aluminum block with dimensions 25 mm x 25 mm x 6 mm. The choice of sample dimensions was arbitrary. Aluminum was chosen as the material since that is a common material found in the vicinity of focal plane arrays. As it turned out, the aluminum windows on the dewar shields provided secondary particle emission comparable to the Al block sample.

A HgCdTe infrared detector array with ~5 μm cutoff wavelength and 1024 x 1024 pixel format was used as the particle detector. The detector array had 4 reference columns at two edges, giving an effective active pixel format of 1024 x 1016. The pixel pitch was 18 μm and the active thickness was ~10 μm. The detector array had the substrate completely removed, so the active volume had essentially no 'dead layer'. In addition, because the detector was in the vacuum of the dewar, the sensitivity to very low range particles was enhanced. These facts make this a unique measurement since most particle detectors do not have sensitivity to very low, micron-range particles. However, the high LET of very low range particles make them problematic for IR detectors that are concerned with low noise levels, as in astronomy applications.

For the particular readout and data acquisition system setup, the detectors had an effective conversion gain of 48.5 μV/e. For the 5 μm cutoff detector $Hg_{1-x}Cd_xTe$ (x = 0.3) material, the ionization energy is ~1.5 eV / carrier pair. We report the results in terms of energy deposition in units of keV using the conversion $48.5 / 1.5 \times 10^{-3} = 3.23 \times 10^4$ μV/keV.

The detector array was located in a low-background cryogenic test dewar with special modifications to allow for the proton beam to pass through the dewar walls with minimum energy loss and with minimum activation of the dewar. The experimental setup is shown in Fig.1 (side view) and Fig. 2 (top view). The cryogenic dewar had thin (125 μm) Kapton vacuum-wall windows on six sides that were lined up with thin (125 μm) Al windows on the interior of the vacuum shroud and on the 2 inner thermal shields. Passing from the outside of the dewar to the detector included 3 Al windows for a total thickness of 375 μm, resulting in a total energy loss through the windows of about 0.8 MeV for the 63 MeV protons. By rotating and positioning the dewar, this arrangement allowed the proton beam to pass into and out of the dewar through the windows on various paths identified in Fig. 2.

For the 'detector path' the beam passed through the IR detector at normal incidence and out the thin window behind the detector. For the 'sample path', the beam passed through the Al sample but did not hit the detector. The sample was located ~7.5 cm from the detector at an angle of ~45 degrees from the normal to the detector. As a control, the 'clear path' was designed to allow the beam to pass through the dewar without hitting the sample or the detector. Comparison of data from the sample path and the clear path allows us to distinguish secondary emissions off the sample from emissions off the interior of the dewar. As an additional control, we took data with the beam missing the dewar and detector completely, but passing nearby (side path).

The detector pulse height distribution data for the clear path, sample path and side path were acquired in a full frame readout mode using a correlated double sampling (CDS) technique. The scan time of 5 ms/row resulted in a rolling readout with an array scan time of 5.12 s for the 1024 x 1024 array. In addition, in order to integrate signal, a 10 s delay separated the two

CDS sample scans so that for a given pixel the effective integration time was 15.12 s. For most data runs, beam was incident on the array continuously for a 300 s interval, with frames acquired continuously for a period of about 330 seconds to provide baseline frames both before the start of the beam and after stop of the beam. Hence for each test sequence (run) about 13 frames were taken with beam continuously present, and a subset of these are reported here.

The data for the detector path were acquired as part of the primary experiment that was optimized for studying transients. For the transient tests, data were acquired in a 20 x 92 subarray that was read repeatedly during beam exposure and stored as data patches in a large array. This data capture scheme is referred as 'quilt mode'. For each frame, there were two reads with the difference between the first read after reset and the second and final read recorded, i.e., CDS with no delay. The effective integration time was 100 ms. The scheme of using repeated reads of a small subarray allowed us to evaluate transient recovery time in the primary experiment. We use that data and extrapolate the subarray data for the detector path to the full frame data taken for the secondary particle paths on the basis of relative fluences, integration times and active areas, as discussed below.

The key parameters for the data runs discussed in this paper are given in Table 1.

III. DATA REDUCTION AND PROCESSING

The distribution of charge deposits in the detector array is related to the distribution of energy losses from the particles that hit the detector during the integration period. The detector array pixels had significant charge sharing (particle-induced cross-talk) between the struck pixel and the neighboring pixels. Charge sharing by diffusion from the hit pixel to neighboring pixels appears to be an important mechanism in large format IR detector arrays for the single particle environment [2,3]. For this experiment, we want to determine the total charge in each hit, including the charge in the struck pixel and the charge that spreads to neighboring pixels. To address this issue, we developed Interactive Data Language (IDL) algorithms to identify hit pixels and sum the total

charge for each hit. All the data reported here is for the total charge in the hit and for many of the hits, the charge is spread over several pixels in the array.

The full frame data required considerable post-processing to remove fixed pattern 'herringbone' noise and other spatial output variations across the array. The sequence for post-processing the data was as follows. First the data was converted to Flexible Image Transfer System (FITS) file format. The FITS file data was then processed with noise filtering algorithms written in IDL code. The dark frames acquired before the beam was turned on were averaged together to create a super bias. This bias was subtracted from the exposures taken with the beam on as a first order baseline correction. On a row by row basis a Gaussian fit to the signal distribution was used to determine a mean and standard deviation. The baseline of each row was mean-centered. A threshold for single event identification was set at 5 times the standard deviation Single events were identified and neighboring pixels (to the central hit) were examined. These neighbors were counted into the total for a given single event sum if they exceeded a value of 250 e- (for runs 20 and 21) and 150 e- (for run 26), which was approximately 5 sigma in each case. Single events identified in each exposure were combined into one array for each run. There were about 75,000 single events per file and 5 files per run, which amounts to around 375,000 events total. Then a histogram of these single events was created using a bin size of 100 e-.

IV. RESULTS AND DISCUSSION

The key experimental results are presented in Figures 3 to 6. The data show pulse height distributions (histograms of number of events versus deposited energy in keV for the array of detector pixels) for several integration periods (frames).

For the sample path (Fig. 3), the collimated proton beam passes through the dewar along a trajectory through thin Al windows and through the Al block, but misses the detector entirely. The energy deposition events recorded in the detector are due to secondary particles from the interaction of the proton beam with the Al block and the Al windows on the dewar walls. These data were taken in full frame mode with the

combined results for 5 frames plotted here. Both differential and integral distributions are shown.

Fig. 4 shows similar data for the clear path, where the proton beam passes through the dewar on a trajectory that misses the Al block and the detector. The only material that the beam passes through is the thin windows on the dewar shields. We detected a large number of secondary particles when the beam misses both the sample and the detector. These are believed to be due to secondary particle emission off the interior of the thin Al windows in the dewar. There are somewhat fewer events in the 100 to 1000 keV range for the clear path than for the sample path.

As a control on the experiment, the dewar was moved just outside the beam and data was acquired in the same manner while the cyclotron was running but the beam was barely missing the dewar. The absence of any significant number of pulses recorded with the cyclotron running (Fig. 5) demonstrates conclusively that the effects seen for the sample path and the clear path were due to secondary particles emitted from surfaces inside the dewar and reaching the detector. The few pulses that were seen above the noise threshold might be due to penetrating neutrons or gammas generated from the operation of the cyclotron, or from noise in the data reduction process.

Fig. 6 shows the detector path where the 63 MeV proton beam is incident on the detector at normal incidence. These pulses are dominated by direct proton hits but obviously must also include the secondary particles. In this case, the data were taken in quilt mode.

To make quantitative comparison of the various histograms, we need to normalize to a common fluence and account for the different integration times, different number of pixels and different active areas of the detector when used in full frame mode (1024 x 1016 pixels, giving 3.37 cm^2) and in quilt mode (20 x 92 pixels, giving 5.96x10^{-3} cm^2). Our approach was to scale the detector histogram (Run 19) to the same effective flux, integration time and number of pixels as for the clear run (20) and sample run (21). The normalization factors are defined in Table 2, and the result is a factor of 7.99x10^3. That is, we multiply the quilt mode data for Run 19 by 7.99x10^3 to be equivalent to the full frame data of Runs 20 and 21.

The composite plot of the integral distributions with the detector run normalized to the sample and clear runs is given in Fig. 7. At the lower energy range, the results show the ratio for scaled direct hits to secondary hits at ~300. Above about 50 keV, the ratio for direct hits to secondary hits is ~10. The scaled detector histogram appears to have a similar slope to the sample and clear histograms at the high end range (e.g., 100 - 500 keV). The lower fluence and number of pixels sampled for the detector run did not allow us to see the higher energy (>500 keV), but low probability pulses, that are due to the secondary particles that accompany the primary particles.

V. ANALYSIS AND MODELING

The observed energy depositions from the secondary particles are consistent with expectations if the particles were delta electrons and scattered protons. Fig. 8 shows the linear charge transfer for electrons and protons in HgCdTe. We note that a 30 keV electron would deposit about the same energy as a 60 MeV proton. Thus, the detector could not distinguish between a 60 MeV primary proton and a 30 keV secondary electron.

While lower energy particles have higher LET when the Bragg peak is approached, the range is decreasing and this factor must be considered for the actual energy deposition in the stopping material. Fig. 9 shows the energy deposited in a 10 μm path of HgCdTe due to protons and electrons. When the particle range is less than the pathlength through the target, the particle's total energy is lost to the target. For a 10 μm path, typical for the detector used in this experiment, we note that the peak energy deposition occurs for ~ 1 MeV protons and ~ 30 keV electrons.

We have performed first order modeling of the expected energy depositions from secondary particles under the particular conditions of the test dewar geometry and the 63 MeV proton beam on the Al sample. The modeling was performed with the transport code NOVICE, which allows detailed 3-dimensional descriptions of the dewar geometry and performs an adjoint Monte Carlo calculation of particle transport

through the surrounding material to the target [4]. Delta electron production was added to the NOVICE code to address the secondary particle issue. The calculation assumed an 18 x 18 x 10 micron pixel of HgCdTe with ionization energy of 1.5 eV per carrier pair. Detailed computer-aided-design drawings of the dewar configuration (see Fig. 2) were modeled with the NOVICE code. The analysis was performed for 63 MeV protons incident on the dewar through the sample path, i.e., the beam on the Al block. Results are presented in terms of histograms of energy deposition events on a per-pixel basis and normalized to 1 p/cm^2. Fig. 10 shows the predicted energy deposition events in the pixel due to delta electrons and to scattered protons from the primary beam incident on the Al sample in the dewar. We note that for the 63 MeV protons, there is an energy deposition cutoff due to delta electrons above about 80 keV and that the energy depositions due to scattered protons peak at about 100 keV.

In Fig. 11, we combine the events from delta electrons and scattered protons, consider the number of pixels and the proton fluence in the measurement, and present the integral distribution. We also show the measured data for the sample path. The drop in the curve around 50 keV is due to the upper energy bound of the secondary electrons. A similar 'knee' is seen in the test data (figures 3 and 4). The model data are compared to the experimental data for the sample path (Run 21) in Table 3. We see reasonably good agreement in the 50 to 100 keV range, with the model predictions higher than measurement by a factor of ~15 at the low end of the distribution and by a factor of ~10 at the high end. The first order model does not account for charge spreading to multiple pixels and this may account for some of the discrepancy.

VI. SUMMARY AND CONCLUSIONS

The experimental data conclusively show that secondary particles emitted from material within the test dewar hit the detector when the proton beam misses the detector. At energies in the 1 to 20 keV range, secondary particles arrive at a rate ~1/300 of the rate for direct proton hits to the detector. At energies above 50 keV, secondary particles arrive at a rate ~1/10 of the rate for direct proton hits. Note that these ratios can only be applied for the particular dewar configuration,

particle energies and beam paths studied in this experiment

The NOVICE transport code, with modifications to include delta electrons, was used to provide a first order prediction of charge deposition in the detectors due to secondary electrons and scattered protons. Comparison of the model to measurements shows good agreement with respect to shape of the energy deposition distributions, reasonable agreement in the mid-energy ranges from 50 to 200 keV, but shows somewhat higher rates than measured at the low and high ends of the distribution.

To our knowledge, this is the first direct measurement of the proton-induced secondary particle environment in the vicinity of an IR detector on a focal plane. This measurement is unique because the detectors are operating in a vacuum and have no surface 'dead layers', resulting in sensitivity to electrons with very low range but high LET. Further work is needed to extend the measurements to lower energies and improve and validate the prediction model in order to better assess the impact on performance of sensors.

VIII. REFERENCES

1. A.Claret, H.Dzitko, and J.J.Engelmann, "Transient Particle Effects on the ISOCAM Instrument On-board the Infrared Space Observatory," "IEEE Trans. Nucl. Sci., Vol. 49, p. 1511, Dec. 1999.
2. R.Ladbury, J.C.Pickel, G.Gee, T.M.Jordan, L.Bergeron, B.Rauscher, R.A.Reed, P.W.Marshall, D.Figer, B.Fodness and S.Kniffen, "Characteristics of the Hubble Space Telescope's Radiation Environment Inferred from Charge Collection Modeling of Near-Infrared Camera and Multi-Object Spectrometer Darkframes," IEEE Trans. Nucl. Sci., Vol. 49, p. 2765, Dec. 2002.
3. J.C.Pickel, R.A.Reed, R.Ladbury, B.Rauscher, P.W.Marshall, T.M.Jordan, B.Fodness and G.Gee, "Radiation-Induced Charge Collection in Infrared Detector Arrays," IEEE Trans. Nucl. Sci., Vol. 49, p. 3822, Dec. 2002.
4. T.M.Jordan, "An Adjoint Charged Particle Transport Method," IEEE Trans. Nucl. Sci., Vol. 23, p. 1857, Dec. 1976.
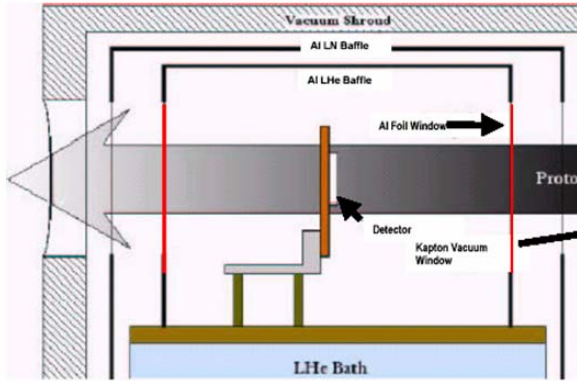
Fig. 1. Schematic view of the test geometry. The detector is held at cryogenic temperature within a vacuum chamber and surrounded by two concentric heat shields. The beam enters and exits the dewar through thin windows in the vacuum and heat shields.
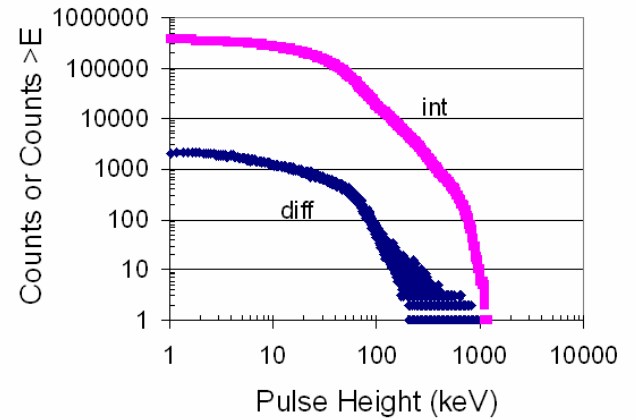
Fig. 3. Distribution of charge deposits for beam hitting the Al sample but not the detector (Sample Path).
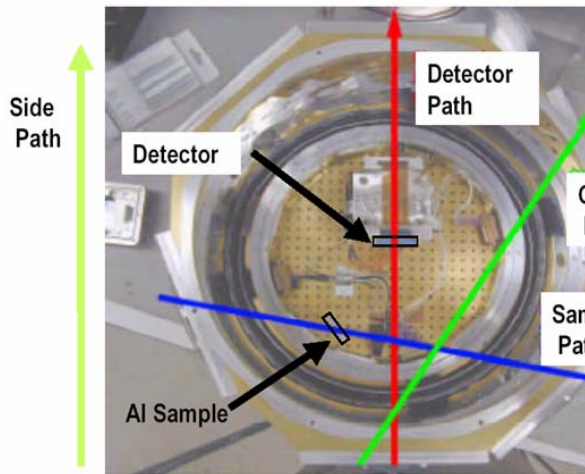

Fig. 4. Distribution of charge deposits for proton beam hitting the dewar but missing the Al sample and the detector (Clear Path).

Fig. 2. Top view showing various beam paths. The Detector Path puts the beam through the detector. The Sample Path puts the beam through an aluminum sample but misses the detector. The Clear Path puts the beam through the dewar, hitting only thin windows, but missing the detector and sample. The Side Path misses the dewar entirely but passes nearby.
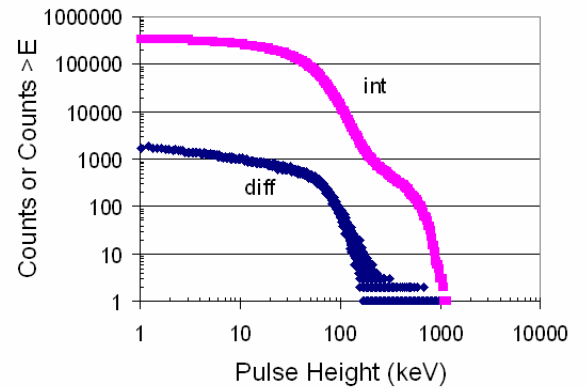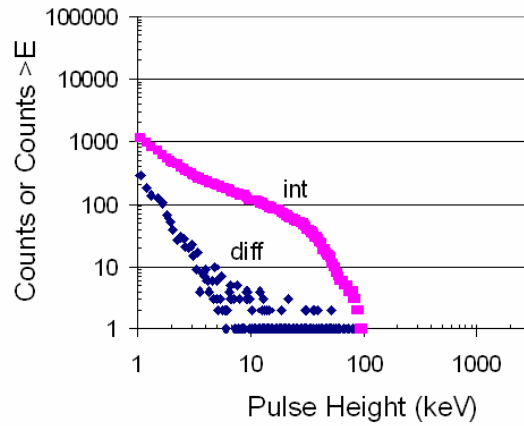
Fig. 5. Beam passing near the dewar but missing the dewar. The absence of a significant number of counts shows that penetrating radiation such as x-rays or neutrons from the cyclotron is not a factor in the previously shown data.
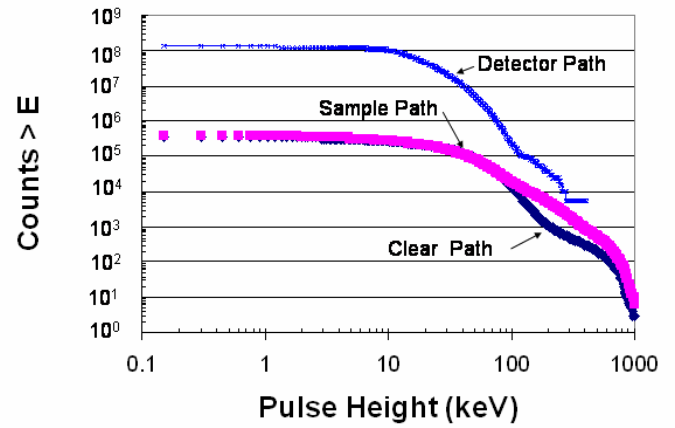
Fig. 7. Composite plot comparing direct proton hits to the detector to secondary particle hits. The detector histogram was scaled up by a factor of 7.99×10^3 to be equivalent to the secondary particle histograms.
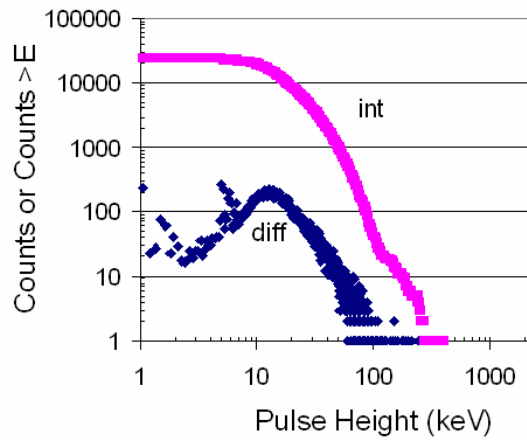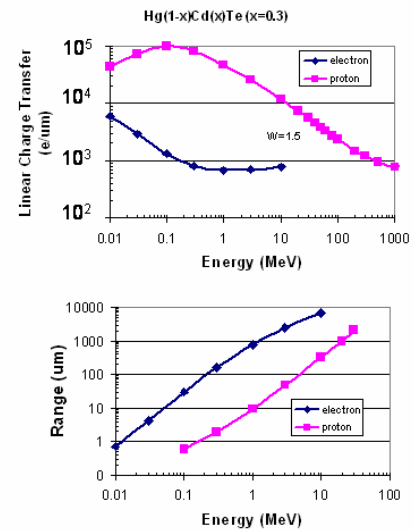

Fig. 6. Proton beam normally incident on the detector.

Fig. 8. Linear charge transfer and range versus energy for protons and electrons in $Hg_{1-x}Cd_xTe$ (x=0.3). An ionization energy of 1.5 eV/e was used.

10 um path of Hg(1-x)Cd(x)Te (x=0.3)
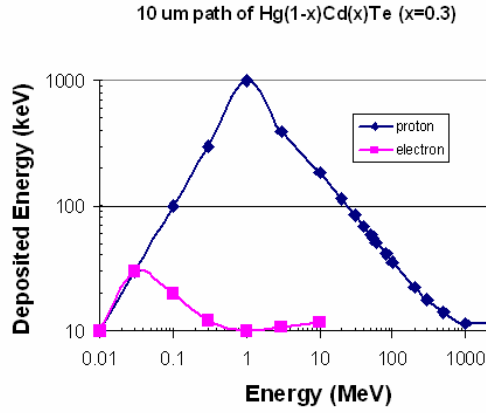

Fig. 9. Energy deposition in 10 um path in Hg1-xCdxTe (x=0.3).

Fig. 11. Model prediction for combined (delta electron and scattered proton) integral distribution of energy deposition events in 18x18x10 micron HgCdTe pixels within the test dewar for 63 MeV protons on the sample path. Model predictions are compared to measured data for the sample path.
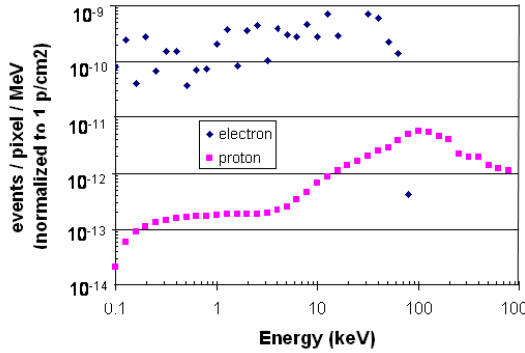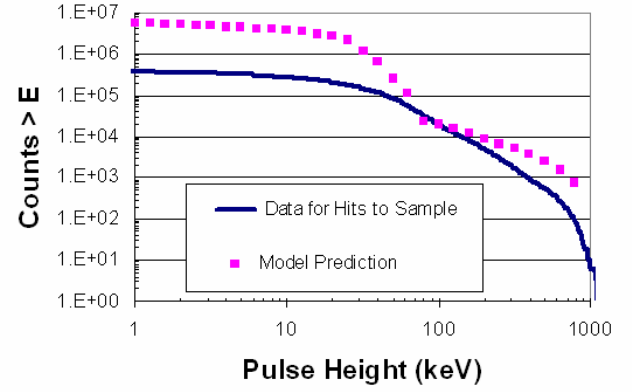
TABLE 1. RUN PARAMETERS

Fig. 10. Model predictions for energy deposition in 18x18x10 micron HgCdTe pixels due to delta electrons and to scattered protons in the test dewar for 63 MeV protons on the sample path.

Path	Run #	Mode	# Pixels /Frame	Active Area (cm²)	# Frames	~Flux p/cm²-s	~Fluence p/cm²
Detector	19	Quilt	1.84×10^3	5.96×10^{-3}	1600	4.07×10^4	4.21×10^6
Clear	20	Full Frame	1.04×10^6	3.37×10^0	5	1.67×10^6	1.26×10^8
Sample	21	Full Frame	1.04×10^6	3.37×10^0	5	1.67×10^6	1.26×10^8
Side	26	Full Frame	1.04×10^6	3.37×10^0	8	7.24×10^4	8.72×10^6

TABLE 2. NORMALIZATION FACTORS.

Run	19	20, 21
# array pixels	1.84×10^3	1.04×10^6
# frames	1600	4
# pixels	2.94×10^6	5.20×10^6
Int Time (s)	0.1	15.12
# pixels * Int Time	2.94×10^5	7.86×10^7
Fluence (p/cm^2)	4.21×10^6	1.26×10^8
Relative Rate	1.24×10^{12}	9.91×10^{15}

TABLE 3. COMPARISON OF MODEL PREDICTIONS AND
MEASUREMENT (SAMPLE PATH)

E (keV)	Model (events/pixel/cm^2)	Predictions for Sample Path	Measured for Sample Path	Ratio predicted/ measured
1	8.71×10^{-9}	5.71×10^6	3.70×10^5	15.42
10	5.67×10^{-9}	3.71×10^6	2.73×10^5	13.61
20	4.38×10^{-9}	2.87×10^6	2.03×10^5	14.14
50	4.00×10^{-10}	2.62×10^5	8.30×10^4	3.16
63	1.78×10^{-10}	1.17×10^5	5.37×10^4	2.17
79	3.50×10^{-11}	2.29×10^4	3.25×10^4	0.71
100	2.90×10^{-11}	1.90×10^4	1.93×10^4	0.98
500	3.70×10^{-12}	2.42×10^3	5.39×10^2	4.50
794	1.13×10^{-12}	7.40×10^2	8.20×10^1	9.03